Communications in Nonlinear Science and Numerical Simulation 126 (2023) 107495

Contents lists available at ScienceDirect

Communications in Nonlinear Science and Numerical Simulation

journal homepage: www.elsevier.com/locate/cnsns

Research paper

Influence of symmetric/asymmetric boundaries on axisymmetric convection in a cylindrical enclosure in the presence of a weak vertical throughflow

P.G. Siddheshwar [a,*], Kanchana C. [b], L.M. Pérez [c], D. Laroze [b]

[a] *Centre for Mathematical Needs, Department of Mathematics, CHRIST(Deemed to be University), Bengaluru 560029, India*
[b] *Instituto de Alta Investigación, Universidad de Tarapacá, Casilla 7 D, Arica 1000000, Chile*
[c] *Departamento de Física, FACI, Universidad de Tarapacá, Casilla 7 D, Arica 1000000, Chile*

ARTICLE INFO

Article history:
Received 5 May 2023
Received in revised form 29 July 2023
Accepted 6 August 2023
Available online 10 August 2023

Keywords:
Axisymmetric convection
Chaos
Cylindrical enclosure
Newtonian-Boussinesq fluid
Rayleigh–Bénard convection
Throughflow

ABSTRACT

The linear and nonlinear stability of axisymmetric convection of a viscous fluid in a cylindrical enclosure heated from below is investigated for various radius to height ratios. A weak vertical throughflow is imposed in a gravity-aligned or a gravity-opposing manner. Symmetric and asymmetric boundaries of free-free, rigid-rigid and rigid-free types are considered for lower and upper boundaries with isothermal temperature boundary condition. The side-walls are assumed to be rigid and adiabatic. A convergent Maclaurin series representation is considered for the finding of axial trial eigenfunctions. In order to corroborate the results of the present study with those of a previous investigation, the critical Rayleigh number and the number of radial rolls manifesting for any given aspect ratio are determined in the case of no throughflow and an exact match is found. Further, the influence of boundaries and the effect of throughflow on chaotic and periodic regimes of motion are studied with the help of a time series solution and the largest Lyapunov exponent as indicators of chaos. The novelty of the present study is the use of a Maclaurin series representation for the eigenfunctions of the linear problem and using the same in determining the solution with the convective mode.

1. Introduction

A physical model which is conceptionally rich and accessible to experiment always remains one of the most actively and extensively studied system. One such system is that of Rayleigh–Bénard convection in a rectangular geometry of infinite horizontal extent where the convection is due to lower boundary being hotter than the upper one. Such a convection is said to be cellular because a pattern of thermally induced vortical motion is observed [1]. The onset of cellular pattern is characterized by a non-dimensional parameter called the critical Rayleigh number (Ra_c). This critical value greatly depends on the type of boundary condition prevalent at the bounding plane surfaces. For instance, Pellew and Southwell [2] considered three distinct thermally conducting boundary conditions at both boundaries: free or rigid, or free top and bottom rigid. They showed that $Ra_c = 657.5, 1707.8$ and 1100.65 respectively for the first, second and third boundary combinations.

Convection in a silicon oil constrained by lateral boundaries of different geometries was demonstrated experimentally by Soberman [3]. He showed that in addition to horizontal boundaries, the critical Rayleigh number is also influenced by

* Corresponding author.
E-mail address: pg.siddheshwar@christuniversity.in (P.G. Siddheshwar).

https://doi.org/10.1016/j.cnsns.2023.107495
1007-5704/

the spacing and the geometry of lateral boundaries. Thermal instability in a viscous fluid constrained by an infinite circular cylinder was investigated by Yih [4]. He considered the physically realistic rigid and adiabatic boundaries. Ostrach and Pnueli [5] considered perfectly conducting boundaries of cylinders of arbitrary cross-section. The primary motivation of the studies of Yih [4], and Ostrach and Pnueli [5] was to report the boundary effect on the value of the critical Rayleigh number. Catton and Edwards [6] considered finite circular cylinders with either perfectly adiabatic or conducting boundaries and showed that the critical Rayleigh number of the perfecting conducting side walls is three times larger than that of the case of adiabatic side walls. Liang et al. [7] considered temperature-dependent viscosity for the axisymmetric buoyancy-driven convective flow in a cylindrical cell bounded by rigid, insulating lateral boundaries and isothermal top and bottom planes. They showed that for a fluid having a variable viscosity, subcritical flows exist with only one of the steady-state solutions remaining stable. Their [7] study is, however, confined to a very narrow range of Rayleigh numbers, beyond which both solutions are equally stable for those values of the Rayleigh number for which axisymmetric motions occur. Using the Rayleigh–Ritz method, Charlson and Sani [8] reported upper and lower bounds on the Rayleigh number for the axisymmetric convection problem in a cylindrical geometry for various radius-to-height ratios.

The critical Rayleigh number can be expressed as a function of the radius-to-height ratio (aspect ratio) of the axisymmetric vertical cylinder. This problem was experimentally investigated by Stork and Müller [9]. They reported the influence of lateral walls of different thermal conductivities and boundary wall thicknesses on the onset of convection. Finite amplitude convection in a shallow cylindrical container with an imperfectly insulated side wall was investigated by Brown and Stewartson [10]. They found a singularity which develops in the amplitude function as the centre of the cylinder is approached, which results in a large cell amplitude at the origin. The transition from a steady flow to an oscillatory flow in unit aspect ratio cylindrical convection was reported by Wang et al. [11] for small Rayleigh and Prandtl numbers. The critical Rayleigh number decreases asymptotically for an increase in the value of the aspect ratio. This was shown by Yu et al. [12] for a circular cylindrical convection problem. Recently, Li et al. [13] observed that the heat transport of the convective system in a cylinder gets enhanced with increase in the aspect ratio for a fixed value of the Rayleigh number.

The effect of adverse vertical temperature gradient, along with imposed vertical mass flux downwards through the layer can be observed in the earth's atmosphere and below cloud base [14,15]. The applicability of this type of mathematical model in the earth's atmosphere was demonstrated by Krishnamurti [16] using a laboratory experimental test for a Boussinesq fluid between two conducting boundaries in the presence of a uniform vertical velocity. The critical Rayleigh number was seen to be increased by a term proportional to Pe^2, the square of the Peclet number, for large Prandtl number, but it decreases by Pe^2 for small Prandtl number. The Peclet number characterizes injection and suction of the fluid through the boundaries. The size of the cell is squashed upward or downward depending upon the sign of Pe being positive or negative.

The influence of a homogeneous inward flow (injection) of fluid at the lower rigid, conducting boundary and outward flow (suction) of fluid at the upper rigid, conducting boundary on the value of critical Rayleigh number in the horizontal extent fluid layer was investigated by Gershuni et al. [17]. Shvartsblat [18] showed that Ra_c increases as Pe increases and thereby argued that the influence of permeable boundaries is to delay the convective instability. Nield reported that the argument of Shvartsblat [18] was deceptive because the influence of permeable boundaries greatly depends on the nature of boundaries. Using an appropriate Fourier-Galerkin expansion, Nield [19] reported asymptotic relations between Ra and Pe for 12 different boundary conditions; FIRI/RIFI, RAFA/FARA, RIRA/RARI, RIFA/FARI, RAFI/FIRA, FIFA/FAFI, where F, R, I, and A denote the free, rigid, isothermal (conducting) and insulating (adiabatic) boundaries. Further, he showed that the stabilizing effect of throughflow ceases when the upper and lower boundaries are asymmetric and when the Prandtl number, Pr, was less than or greater than 5/4. Thereby, he showed the importance of Pr and the nature of boundaries in throughflow problems. Very recently there is a reported work by Capone et al. [20] on weakly nonlinear Darcy-Bénard convection with throughflow of a Newtonian-Boussinesq fluid but this fluid system is housed in a rectangular geometry and considers symmetric boundaries. The influence of the vertical throughflow on the critical Rayleigh number, aspect ratio of the cylinder and the geometry of the cylindrical cross-section was reported by Barletta and Storesletten [21] in a vertical porous cylinder with a permeable and conducting side boundary. An extension of this study to a power law fluid was made by Brandão [22].

In the present paper, we consider the combined influence of a weak throughflow on linear and weakly nonlinear stability analyses of axisymmetric convection of a viscous fluid in cylindrical enclosures heated from below with boundaries being either symmetric or asymmetric. A range of radius to height aspect ratios is considered. The lateral boundaries are assumed to be rigid and adiabatic (as reported by Charlson and Sani [8]). Using the Maclaurin series representation, the axial trial eigenfunctions are obtained. In order to corroborate the results obtained in the paper with earlier findings, comparison is made for the limiting case of no throughflow. An exact match is found between the plots of Ra_c versus r_0, the aspect ratio, for rigid isothermal boundaries of the present study with those of Charlson and Sani's work [8]. Further, the dynamical behaviour of the system is analysed using the largest Lyapunov exponent (LLE) and the time series solution. The drastic change in the influence of the throughflow due to an asymmetric boundary condition is explained. The present paper makes a linear and nonlinear stability analyses of cylindrical Rayleigh-Bénard convection in the presence of a weak throughflow, and considers both symmetric and asymmetric boundary combinations.

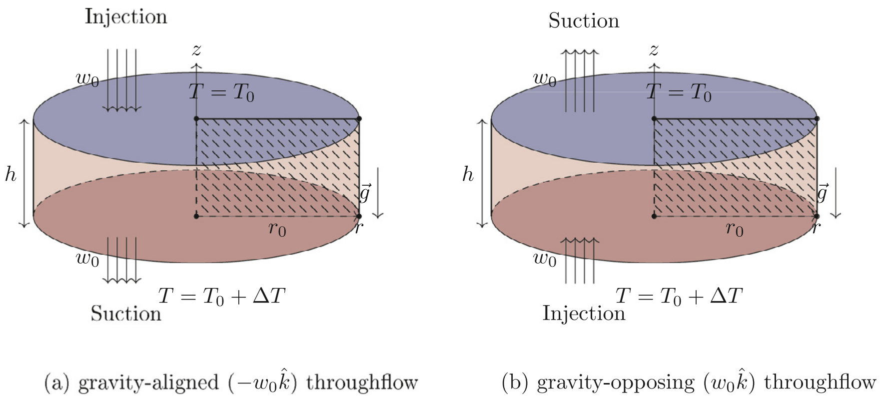

Fig. 1. Schematic of axisymmetric convection in a cylindrical enclosure in the presence of vertical throughflow with radius, r_0, and height, h. Here $w_0(>0)$ is the prescribed throughflow velocity that is vertically downwards or upwards.

2. Mathematical formulation

Consider a cylindrical enclosure of height h and radius r_0 occupied by a Boussinesq fluid. The fluid is assumed to be of constant viscosity and thermal diffusivity with its density varying linearly with temperature. The lower and upper circular plates are maintained at constant temperatures $T_0 + \Delta T(\Delta T > 0)$ and T_0 respectively. A throughflow is imposed at upper and lower plates in a gravity-aligned or a gravity-opposing manner as shown in Fig. 1.

The governing equations for the aforementioned set up are [11]:

$$\nabla \cdot \vec{q} = 0, \tag{1}$$

$$\rho_0 \frac{\partial \vec{q}}{\partial t} = -\nabla p + \mu \nabla^2 \vec{q} + \rho_0 \left[1 - \beta \left(T - T_0\right)\right] \vec{g}, \tag{2}$$

$$\frac{\partial T}{\partial t} + \vec{q} \cdot \nabla T = \kappa \nabla^2 T, \tag{3}$$

where $\nabla = \hat{e}_r \dfrac{\partial}{\partial r} + \hat{e}_z \dfrac{\partial}{\partial z}$, $\hat{e}_r$ and $\hat{e}_z$ are unit vectors along radial (r) and vertical (z) axes, $\nabla^2 = \dfrac{\partial^2}{\partial r^2} + \dfrac{1}{r}\dfrac{\partial}{\partial r} + \dfrac{\partial^2}{\partial z^2}$ is the Laplacian operator in cylindrical coordinate system, $\vec{q} = (u,\ w)$ is the two-dimensional velocity vector, $\rho_{nl}(T)$ is the density, $\rho_{nl_0} = \rho_{nl}(T_0)$ is the reference density, t is the time, p is the dynamic pressure, $\vec{g} = -g\hat{k}$ is the acceleration due to gravity, T is the temperature and κ is the thermal diffusivity of the fluid. In writing Eq. (2), we have neglected the non-linear term, $(\vec{q} \cdot \nabla)\vec{q}$, by assuming small scale convective motion.

The Eqs. (1)–(3) are first solved subject to following conditions in the basic state:

$$\left.\begin{aligned} w = w_0,\ T = T_0 \text{ at } z = h \\ w = w_0,\ T = T_0 + \Delta T \text{ at } z = 0 \end{aligned}\right\},\ r < r_0, \tag{4}$$

We assume the following boundary condition (see Eq. (38) of Charlson and Sani [8]) at the lateral boundaries:

$$u = \frac{\partial T}{\partial r} = 0 \text{ at } r = r_0,\ 0 \le z \le h. \tag{5}$$

The motionless conduction solution of the governing Eqs. (1)–(3) is as given below:

$$\left.\begin{aligned} \vec{q}_b = (0, w_0),\ T = T_b(z) = T_0 + \Delta T\ \mathtt{f}(z), \\ p_b(z) = -\int \rho_b(z) g dz + c, \quad \rho_b(z) = \rho_0 \left[1 - \beta \Delta T \mathtt{f}(z)\right], \end{aligned}\right\} \tag{6}$$

where w_0 is the prescribed vertical throughflow velocity, $\mathtt{f}(z) = (e^{Pe} - e^{Pe\frac{z}{h}})/(e^{Pe} - 1)$, c is the constant of integration and $Pe = w_0 h/\kappa$ is the Peclet number which characterizes the vertical throughflow of the fluid.

Superimposing the following thermal perturbation on the basic state:

$$\vec{q} = \vec{q}_b + \vec{q}',\ T = T_b(z) + T',\ \rho = \rho_b(z) + \rho',\ p = p_b(z) + p', \tag{7}$$

eliminating the pressure in the perturbed form of Eq. (2), incorporating the quiescent state solution and non-dimensionalizing the resulting equation using the following scaling:

$$(u^*, w^*) = \frac{h}{\kappa}(u', w'), \quad T^* = \frac{T'}{\Delta T}, \quad (r^*, z^*) = \frac{1}{h}(r, z), \quad t^* = \frac{\kappa}{h^2}t,\ r_0^* = \frac{r_0}{h}, \tag{8}$$

we get (after omitting asterisks):

$$\nabla \cdot \vec{q} = 0, \tag{9}$$
$$\frac{1}{Pr}\frac{\partial}{\partial t}(\nabla^2 w) = \nabla^4 w + Ra\nabla_1^2 T, \tag{10}$$
$$\frac{\partial T}{\partial t} = g(z)w + \nabla^2 T - Pe\frac{\partial T}{\partial z} - \vec{q}\cdot\nabla T, \tag{11}$$

where $Pr = \mu/(\rho_0\kappa)$ is the Prandtl number, $Ra = (\rho_0\beta g(\Delta T)h^3)/(\mu\kappa)$ is the Rayleigh number and the function $g(z)$ is defined as $g(z) = Pe\, e^{Pez}/(e^{Pe} - 1)$.

The governing Eqs. (9)–(11) of the perturbed state are solved using the following horizontal boundary conditions:

(i) FIFI

$$w = \frac{\partial^2 w}{\partial z^2} = T = 0 \text{ at } z = 0, 1, \quad r < r_0 \tag{12}$$

(ii) RIRI

$$w = \frac{\partial w}{\partial z} = T = 0 \text{ at } z = 0, 1, \quad r < r_0 \tag{13}$$

(iii) FIRI

$$\left.\begin{aligned} w = \frac{\partial w}{\partial z} = T = 0 \text{ at } z = 0 \\ w = \frac{\partial^2 w}{\partial z^2} = T = 0 \text{ at } z = 1 \end{aligned}\right\}, \quad r < r_0 \tag{14}$$

The lateral boundary condition in the perturbed state is:

$$u = \frac{\partial^2 u}{\partial r^2} + \frac{\partial}{\partial r}\left(\frac{u}{r}\right) = \frac{\partial T}{\partial r} = 0, r = r_0, \quad 0 \le z \le 1. \tag{15}$$

We next perform a linear stability analysis using a normal mode solution that involves zeroth and first-order Bessel functions satisfying the lateral boundary condition and also the continuity Eq. (9). The axial trial functions for the velocity and temperature components are determined by using the Maclaurin series. The desired number of terms required in the series is decided upon by using the D Alembert's ratio test.

In the case of the cylindrical RBC problem one can prove the validity of the principle of exchange of stabilities and hence we consider stationary convection in Section 3.

3. Linear stability analysis

The normal mode representation of (u, w, T) for the marginal stationary state is:

$$u = AJ_1(\alpha\, r)F'(z), \tag{16}$$
$$w = AJ_0(\alpha\, r)F(z), \tag{17}$$
$$T = BJ_0(\alpha\, r)G(z), \tag{18}$$

where J_0 and J_1 are the Bessel functions of zeroth- and first-order respectively, α is the wave number, and the prime on the axial eigenfunction denotes $\frac{d}{dz}$.

Substituting Eqs. (16)–(18) into the steady state, linear version of Eqs. (9)–(11), we get

$$\left.\begin{aligned} F'''' - 2\alpha^2 F'' + \alpha^4 F - \alpha Ra G = 0, \\ G'' - \alpha^2 G + \alpha g F - Pe G' = 0 \end{aligned}\right\}, \tag{19}$$

along with the boundary condition:

$$\left.\begin{aligned} &F = F'' = G = 0 \text{ at } z = 0, 1 \text{ for FIFI} \\ &F = F' = G = 0 \text{ at } z = 0, 1 \text{ for RIRI} \\ &\left.\begin{aligned} F = F' = G = 0 \text{ at } z = 0 \\ F = F'' = G = 0 \text{ at } z = 1 \end{aligned}\right\} \text{ for FIRI} \end{aligned}\right\}. \tag{20}$$

We assume the Maclaurin series expansion for the eigenfunctions $F(z)$ and $G(z)$ as:

$$\left.\begin{aligned} F(z) &= \sum_{n=0}^{\infty} c_k z^k, \\ G(z) &= \sum_{n=0}^{\infty} d_k z^k, \end{aligned}\right\} \tag{21}$$

Substituting Eq. (21) into Eq. (19) results in the following recurrence relation:

$$\left.\begin{aligned} (k+4)(k+3)(k+2)(k+1)c_{k+4} \\ -2\alpha^2(k+2)(k+1)c_{k+2} + \alpha^4 c_k - \alpha Ra d_k = 0, \\ (k+2)(k+1)d_{k+2} - \alpha^2 d_k + \alpha g_1 c_k = 0 \end{aligned}\right\}, \tag{22}$$

where $g_1 = Pe/(e^{Pe} - 1)$.

The first few coefficients in the recurrence relation are obtained by using the conditions defined at $z = 0$ in Eq. (20). Using these known terms and Eq. (22), we obtain $F(z)$ and $G(z)$ for different horizontal boundary conditions as follows:

(i) For FIFI, we have

$$\begin{aligned} F(z) &= z + \frac{a_1}{6}z^3 - \frac{\alpha}{120}(\alpha^3 - 2a_1\alpha - a_2 Ra)z^5 + \frac{\alpha}{720}a_2 Pe\, Ra\, z^6 \\ &\quad - \frac{\alpha}{5040}\left(2\alpha^5 + 3a_1\alpha^3 + 3a_2 Ra\alpha^2 - g_1 Ra\alpha + a_2 Pe\, Ra\right)z^7 \\ &\quad + \cdots + o(z^N), \end{aligned} \tag{23}$$

$$\begin{aligned} G(z) &= a_1 z + \frac{a_2}{2}Pe z^2 + \frac{1}{6}\left(a_2\alpha^2 - g_1\alpha + a_2 Pe^2\right)z^3 \\ &\quad + \frac{Pe}{24}\left(2a_2\alpha^2 - 3g_1\alpha + a_2 Pe^2\right)z^4 + \frac{1}{120} \\ &\quad \left(a_2(\alpha^4 + 2Pe^2\alpha^2 + Pe^4) - g_1\alpha(\alpha^2 + a_1 + 6Pe^2)\right)z^5 \\ &\quad + \cdots + o(z^N), \end{aligned} \tag{24}$$

(ii) For RIRI and FIRI, we have

$$\begin{aligned} F(z) &= \frac{a_1}{2}z^2 + \frac{1}{6}z^3 + \frac{a_1}{12}\alpha^2 z^4 + \frac{\alpha}{120}(2\alpha + a_2 Ra)z^5 + \frac{\alpha}{720} \\ &\quad (3a_1\alpha^3 + a_2 Pe Ra)z^6 + \frac{\alpha}{5040}(3\alpha^3 + a_2 Ra(Pe^2 + 3\alpha))z^7 \\ &\quad + \cdots + o(z^N), \end{aligned} \tag{25}$$

$$\begin{aligned} G(z) &= a_2 z + \frac{a_2}{2}Pe z^2 + \frac{a_2}{6}(\alpha^2 + Pe^2)z^3 + \frac{1}{24}\left(a_1\alpha g_1\right. \\ &\quad \left. + a_2 Pe(Pe^2 + 2\alpha^2)\right)z^4 + \frac{1}{120}(-\alpha g_1(1 + 4a_1 Pe) \\ &\quad + a_2(Pe^4 + 3Pe^2\alpha^2 + \alpha^4))z^5 + \cdots + o(z^N), \end{aligned} \tag{26}$$

where N denotes the number of terms considered in the Maclaurin series. As mentioned earlier, the value of N is decided upon by using the D Alembert's ratio test for testing convergence. In Eqs. (25) and (26), the quantities a_1 and a_2 come from the assumed initial conditions in place of the right end boundary conditions. Further, we note that one normalization is also used in arriving at them. On using the unused three right end boundary conditions we can determine a_1, a_2 and Ra_c for a given value of Pe.

To determine α_c, we use the lateral boundary condition (15), which gives the transcendental equation:

$$J_1(\alpha\, r_0) = 0. \tag{27}$$

It is convenient to use the scaled version of α further on and hence we consider $\alpha r_0 = p$. Thus, from Eq. (27), we now have:

$$J_1(p) = 0. \tag{28}$$

Let $p_1, p_2, \ldots$ be the positive real roots of Eq. (28) which are such that $p_1 < p_2 < p_3 < \cdots$. Corresponding to $p_k's$, we have α_k's such that $p_k = \alpha_k r_0$. For given r_0, we may determine the α_k's from the p_k's.

We next consider a weakly nonlinear stability analysis.

4. Weakly nonlinear stability analysis

To bring in the nonlinear effect, we add a convective mode to the modes considered in the linear stability analysis:

$$u = -\frac{\sqrt{2}\delta^2}{\alpha}\mathcal{X}(t)J_1(\alpha\ r)F'(z), \tag{29}$$

$$w = \frac{\sqrt{2}\delta^2}{\pi\alpha}\mathcal{X}(t)J_0(\alpha\ r)F(z), \tag{30}$$

$$T = \frac{1}{\pi \mathrm{r}}[\mathcal{Y}(t)J_0(\alpha\ r)G(z) + \mathcal{Z}(t)H(z)], \tag{31}$$

where $\delta^2 = (\alpha^2 + \pi^2)$, $\mathrm{r} = \dfrac{Ra}{Ra_c}$ and $H(z)$ is given by

$$H(z) = \int_0^z \left[\int_0^\xi F'(\eta)\ G(\eta)\ d\eta\right] d\xi + m_1 e^{Pez} z, \tag{32}$$

and m_1 is determined using the boundary condition. The terms, $\mathcal{X}(t)$, $\mathcal{Y}(t)$ and $\mathcal{Z}(t)$ represent the time-dependent amplitudes. The scaling used in Eqs. (29)–(31) for the amplitudes are those used in the classical Lorenz model. Substituting Eqs. (29)–(31) into Eqs. (9)–(11) and applying standard orthogonality condition, we get

$$\left.\begin{aligned} \frac{d\mathcal{X}}{d\tau_1} &= Pr(-l_1\mathcal{X} + l_2\mathcal{Y}) \\ \frac{d\mathcal{Y}}{d\tau_1} &= l_3\ \mathrm{r}\ X - p_4 Y - l_5\mathcal{X}\mathcal{Z} \\ \frac{d\mathcal{Z}}{d\tau_1} &= -bl_6\mathcal{Z} + l_7\mathcal{X}\mathcal{Y} \end{aligned}\right\}, \tag{33}$$

where $\tau_1 = \delta^2 t$ and $b = 4\pi^2/\delta^2$. The coefficients l_i's are given by

$$\left.\begin{aligned} & l_1 = -\frac{\langle \alpha^4F^2 + F\dfrac{d^4F}{dz^4} - 2\alpha^2F\dfrac{d^2G}{dz^2}\rangle}{\delta^2\langle -\alpha^2F^2 + F\dfrac{d^2F}{dz^2}\rangle},\quad l_2 = \frac{-\delta^2\langle FG\rangle}{\langle -\alpha^2F^2 + F\dfrac{d^2F}{dz^2}\rangle}, \\ & l_3 = \frac{\langle FG\rangle}{\langle G^2\rangle},\quad l_4 = -\frac{\langle -\alpha^2G^2 + G\dfrac{d^2G}{dz^2}\rangle}{\delta^2\langle G^2\rangle},\quad l_5 = -\frac{1}{\pi}\frac{\langle FG\dfrac{dH}{dz}\rangle}{\langle G^2\rangle}, \\ & l_6 = -\frac{1}{b\delta^2}\frac{\langle H\dfrac{d^2G}{dz^2}\rangle}{\langle H^2\rangle},\quad l_7 = \frac{2}{\pi}\frac{\langle\left(F\dfrac{dG}{dz} + G\dfrac{dF}{dz}\right)F\rangle}{\langle F^2\rangle} \end{aligned}\right\}. \tag{34}$$

We now transform the dynamical system in Eq. (33) into the form of the classical Lorenz model [23] by using an appropriate second scaling for the amplitudes as:

$$\mathcal{X} = s_1X,\ \mathcal{Y} = s_2Y,\ \mathcal{Z} = s_3Z, \tag{35}$$

where $s_1 = l_4/\sqrt{l_5l_7}$, $s_2 = (l_1/l_2)s_1$ and $s_3 = (l_1l_4)/(l_2l_5)$. Substituting Eqs. (35) into Eq. (33), we get the modified Lorenz model that takes the form of the classical Lorenz model [23] with modified definition of non-dimensional parameters and is given by:

$$\left.\begin{aligned} \frac{dX}{d\tau} &= Pr^*(-X + Y), \\ \frac{dY}{d\tau} &= r^*\ X - Y - XZ, \\ \frac{dZ}{d\tau} &= -b^*Z + XY \end{aligned}\right\}, \tag{36}$$

where $\tau = l_4\tau_1$, $Pr^* = (l_1/l_4)Pr$, $b^* = (l_6/l_4)b$ and $r^* = ((l_2l_3)/(l_1l_4))\mathrm{r}$. The modified non-dimensional parameters, Pr^*, b^* and r^* are functions of Pe. From Eq. (36), one can easily obtain the expression of the Hopf Rayleigh number, r_H^*, as given below [23–25]:

$$r_H^* = \frac{Pr^*(Pr^* + b^* + 3)}{Pr^* - b^* - 1}. \tag{37}$$

In what follows, we shall refer to r_H^* as just r_H.

In the literature concerning chaos, a series of indicators are used to study chaos in the dynamical system and one such indicator is the Lyapunov exponent (LE). This quantifies the divergence between the two initially close trajectories of the vector field. The LEs of a system represent the dynamical freedom of the system and thus, the largest Lyapunov exponent (LLE) represents the largest freedom, in the sense that small changes in the past lead to larger changes in the future. To obtain LLE, we denote the generalized Lorenz system (36) as:

$$\frac{d\mathbf{Y}}{d\tau} = M(\mathbf{Y}, \tau) \tag{38}$$

and then the LEs can be obtained as

$$\lambda_i = \lim_{\tau\to\infty}\left[\frac{1}{\tau}Ln\left(\frac{|\delta \mathrm{Y}_i(\tau)|}{|\delta \mathrm{Y}_i(0)|}\right)\right], \tag{39}$$

where λ_i, $i = 1, 2, 3$ (the dimension of the system), are a mean rate of separation of trajectories of the system, $\delta\mathrm{Y}_i(0)$ are the initial separation and $\delta\mathrm{Y}_i(\tau)$ are the separation after time τ. Thus, $\delta\mathrm{Y}_i(\tau)$ satisfy the variational equation

$$\frac{d}{d\tau}(\delta\mathbf{Y}) = \mathbf{J}\cdot\delta\mathbf{Y}, \tag{40}$$

where $\mathbf{J}$ involves quantities of the form $\partial M_i/\partial Y_j$. The largest among the λ_i, $i = 1, 2, 3$, denoted by LLE, is the largest LE which decides the nature of the attractors. If $LLE < 0$ then the trajectory is a fixed point and if $LLE = 0$ then it is a periodic orbit. If $LLE > 0$, then it is a chaotic or a strange attractor. To determine these values, we have numerically integrated the generalized modified Lorenz model using the classical fourth-order Runge–Kutta method with a step size of 0.0005.

5. Discussion of results

5.1. Linear stability analysis

The Maclaurin series representation for the axial trial eigenfunctions was considered with 15, 18 and 22 terms respectively for FIFI, FIRI and RIRI boundaries. The Bessel functions are used as radial trial eigenfunctions. Using these in combination as shown in Eqs. (16)–(18), the Rayleigh number was determined for each value of the aspect ratio, r_0. Fig. 2 shows the lowest neutral stability branch for symmetric and asymmetric boundaries in the parametric plane (r_0, Ra). Depending on the range of r_0, different p_k, $k = 1, 2, 3, \ldots$ give the lowest independent stability curves in the (r_0, Ra) plane. The vertical dashed lines in Fig. 2 represent the transition between these lowest branches as a function of r_0. Since r_0 and α are inversely proportional to each other with p as their product, this indeed means that the transition between the lowest branches depends on the value of α, and thereby r_0 is directly proportional to the wavelength, and hence as r_0 increases the number of cells also increases. In other words, if the number of radial cells is fixed there is always a threshold aspect ratio, $(r_0)_T$, which yields the smallest value of the Rayleigh number, Ra_c. The insets of the clockwise and anticlockwise rotating cells between these vertical lines in Fig. 2 indicate the number of cells that form in that r_0-interval. The curves corresponding to $Pe < 0$ and $Pe > 0$ respectively represent the axisymmetric convection in cylindrical enclosure problems with gravity-aligned and gravity-opposing cases of throughflow while $Pe = 0$ is the corresponding problem with no throughflow. The horizontal line in Fig. 2 denotes the Ra_c value in the limiting case of no throughflow. It is clear from this figure that $Ra \to \infty$ when r_0 approaches zero and r_0 approaching zero means that the height of the cylinder is much larger than its radius. In this case the onset of convection is more and more inhibited as the vertical distance between the horizontal isothermal boundaries becomes larger and larger with increasing r_0, and the cylinder becomes slender. On the other hand, when r_0 approaches infinity, the Ra value at transition point approaches Ra_c, thereby one observes the infinite horizontal extent convection. The critical and transition values of r_0, Ra and α at each marginal curve are documented in Table 1. The stability curve concerns RIRI boundaries in the case of no throughflow reiterates the finding of Charlson and Sani's [8] work.

Fig. 2 and Table 1 also give information about the influence of weak throughflow on the stability of the system. In the case of the symmetric boundaries of FIFI and RIRI, the influence of both gravity-aligned and gravity-opposing types of throughflow is to stabilize the system whereas, in the case of FIRI boundary combination, the influence of gravity-aligned throughflow is to stabilize the system while the influence of gravity-opposing throughflow is to destablize the system.

Although there is noticeable change in the values of Ra_c between the cases of no throughflow and a weak throughflow, the values of Ra and r_0 at each transition remains the same. The influence of weak throughflow on Ra_c is more predominant than that on α_c. Compared to symmetric boundaries of FIFI and RIRI, the influence of throughflow is significant for the asymmetric boundaries of FIRI. This result can be understood by noting that although the vertical throughflow velocity is constant the nature of upper and lower boundaries are different in the case of FIRI and the flow within the system also modifies accordingly leading to advanced/delayed convection depending on whether the throughflow is gravity-aligned or gravity-opposing. Further, Fig. 2 also suggests that compared to the physically realistic boundaries of RIRI and FIRI, in the case of idealistic boundaries of FIFI, the range of r_0 over which a given number of cells (m) is predicted is less. This is because when the boundaries are rigid then the fluid adheres to its bounding surface and hence the velocity of the fluid at a rigid boundary surface is that of the boundary and this aspect is fully utilized in the formation of cells.

In what follows, we discuss the results of a weakly nonlinear stability analysis.

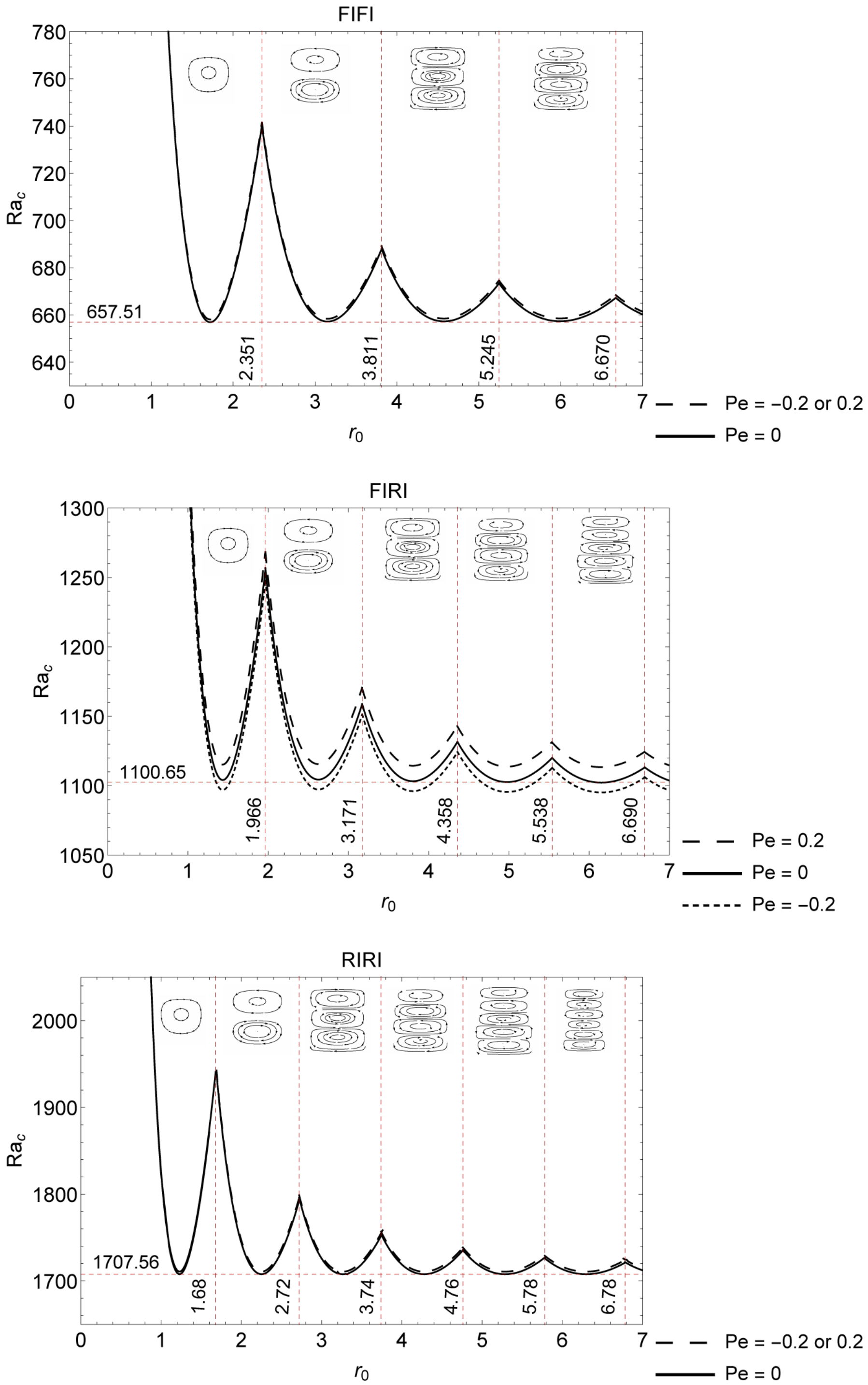

Fig. 2. Plot of Ra_c versus r_0 for different boundaries.

Table 1
The critical and transition values of r_0, Ra and α for each transit branch. Here m denotes the number of cell.

Nature of the boundaries	Pe	m	p	Critical values for marginal curve			Values at transition point		
				$(r_0)_c$	Ra_c	α_c	Ra_T	$(r_0)_T$	α_T
FIFI	0	1	3.83171	1.72	657.51	2.2214	740.413	2.351	1.62982
		2	7.01559	3.16			688.230	3.811	1.84088
		3	10.1735	4.58			673.352	5.245	1.93966
		4	13.3237	6.00			667.256	6.670	1.99756
	± 0.2	1	3.83171	1.72	658.72	2.2243	741.409	2.351	1.62982
		2	7.01559	3.15			689.214	3.811	1.84088
		3	10.1735	4.57			689.214	5.245	1.93966
		4	13.3237	5.99			668.481	6.670	1.99756
FIRI	-0.2	1	3.83171	1.43	1111.69	2.6845	1268.320	1.966	1.94899
		2	7.01559	2.61			1170.540	3.171	2.21242
		3	10.1735	3.79			1143.020	4.358	2.33444
		4	13.3237	4.96			1131.340	5.538	2.40587
		5	16.4706	6.14			1124.360	6.690	2.46197
	0	1	3.83171	1.43	1100.65	2.6800	1255.870	1.966	1.94899
		2	7.01559	2.62			1158.710	3.171	2.21242
		3	10.1735	3.79			1131.620	4.358	2.33444
		4	13.3237	4.97			1120.050	5.538	2.40587
		5	16.4706	6.14			1113.200	6.690	2.46197
	0.2	1	3.83171	1.43	1093.57	2.6820	1247.680	1.966	1.94899
		2	7.01559	2.62			1151.340	3.171	2.21242
		3	10.1735	3.79			1124.320	4.358	2.33444
		4	13.3237	4.97			1112.840	5.538	2.40587
		5	16.4706	6.14			1106.030	6.690	2.46197
RIRI	0	1	3.83171	1.23	1707.76	3.1170	1945.56	1.680	2.28078
		2	7.01559	2.25			1793.66	2.720	2.57926
		3	10.1735	3.26			1795.96	3.740	2.72019
		4	13.3237	4.27			1735.34	4.760	2.79910
		5	16.4706	5.28			1726.98	5.780	2.84958
		6	19.6159	6.29			1721.05	6.780	2.89320
	± 0.2	1	3.83171	1.23	1710.71	3.1190	1948.42	1.680	2.28078
		2	7.01559	2.25			1796.53	2.720	2.57926
		3	10.1735	3.26			1755.84	3.740	2.72019
		4	13.3237	4.27			1738.45	4.760	2.79910
		5	16.4706	5.28			1730.06	5.780	2.84958
		6	19.6159	6.29			1724.11	6.780	2.89320

5.2. Weakly nonlinear stability analysis

The weakly non-linear stability analysis of the present problem leads to a Lorenz model (36) whose form is that of the classical one with modified non-dimensional parameters. In view of this the transition to chaos from the regular convective motion can be written in terms of the Hopf Rayleigh number, r_H, as a function of modified parameters. The analytical expression of r_H is given in Eq. (37). The r_H plots in Fig. 3 for symmetric and asymmetric boundaries are plotted using this expression for different values of Pe. The influence of boundaries on r_H and Ra_c is qualitatively the same, i.e.,

$$r_H^{FIFI} < r_H^{FIRI} < r_H^{RIRI} \text{ and } Ra_c^{FIFI} < Ra_c^{FIRI} < Ra_c^{RIRI}. \tag{41}$$

However, an interesting observation that we extracted from Fig. 3 is that the influence of throughflow on r_H irrespective of whether it is being gravity-aligned or gravity-opposing in the case of symmetric boundaries is exactly opposite to that seen on Ra_c, i.e.,

$$r_H^{Pe=0} > r_H^{Pe\neq 0} \text{ and } Ra_c^{Pe=0} < Ra_c^{Pe\neq 0}. \tag{42}$$

In the case of gravity-aligned throughflow and asymmetric boundaries similar influence to what is shown in Eq. (42) can be observed while in the case of gravity-opposing throughflow the scenario is entirely opposite, i.e.,

$$r_H^{Pe=0} < r_H^{Pe>0} \text{ and } Ra_c^{Pe=0} > Ra_c^{Pe>0}. \tag{43}$$

From the results presented in Eqs. (41)–(43), we may conclude that it is wrong to assume that parameters' influence on the onset of regular and chaotic motions are the same for all boundary combinations.

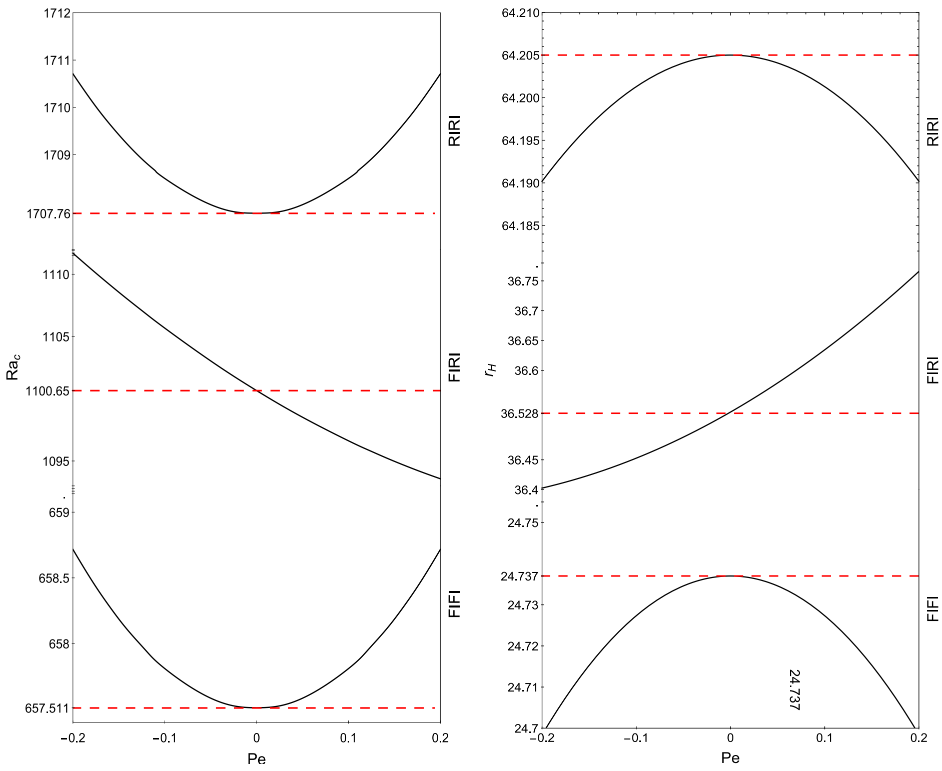

Fig. 3. Plot of Ra_c and r_H versus Pe for different boundaries by taking $r_0 = (r_0)_T$ and $Pr = 10$.

It is also clear from Fig. 3 that the results on the influence of Pe on Ra_c and r_H need separate discussion for symmetric and asymmetric boundaries. In the case of symmetric boundaries FIFI and RIRI, Ra_c and r_H are both even powers of Pe while in the case of asymmetric boundaries it is an odd function.

Once details of the appearance of chaos is confirmed the next interest will be on determining the intensity of the chaos, the possibility of limit cycles and the influence of throughflow and boundaries on these two aspects. This can be studied using various indicators. The LLE and the bifurcation diagram are popularly used indicators because of their accurate prediction, and the commonness between them that makes it easy to use one in place of the other or to reconfirm the result of each other. The procedure and the numerical method used in the paper to determine LLE and to plot the bifurcation diagram are mentioned just before Section 5. Figs. 4 and 5 are the plots of LLE and bifurcation diagrams versus r^* for the cases of $Pe = 0$ and $Pe \neq 0$, and for different boundaries. It is clear from these plots that the value of r^* at which chaos manifests, viz., r_H obtained by using the analytical expression (37) exactly matches with those predicted by the plots obtained by using the numerical integration of the modified Lorenz Eq. (36).

Earlier on in Fig. 3 we observed in the case of symmetric boundaries that the influence of weak throughflow is to postpone the onset of regular convection and prepone the onset of chaotic motion irrespective of the vertical throughflow being gravity-aligned or gravity-opposed. Also, it was observed that in the case of an asymmetric boundary, the influence of gravity-aligned and gravity-opposed throughflow is to prepone and postpone the onset of chaotic motion respectively. This finding is due to the fact that r_H is even and an odd function of Pe respectively in the case of symmetric and asymmetric boundaries. In addition to these results predicted by the bifurcation diagrams too in Figs. 4 and 5, they predict the preponement and suppression respectively of the appearance of periodic motion in the cases of gravity-aligned and gravity opposed throghflows, for the case of asymmetric boundaries. Suppression of periodic motion implies preference for chaotic motion (termed as intense chaotic motion). In the case of symmetric boundaries the scenario seen in the case of no throughflow appears translated in the presence of both types of throughflow.

The similarity or dissimilarity in the dynamics described by the bifurcation diagram due to the throughflow occurs mainly at the periodic points/intervals. In the case of RIRI boundaries, the number of periodic points/intervals is less

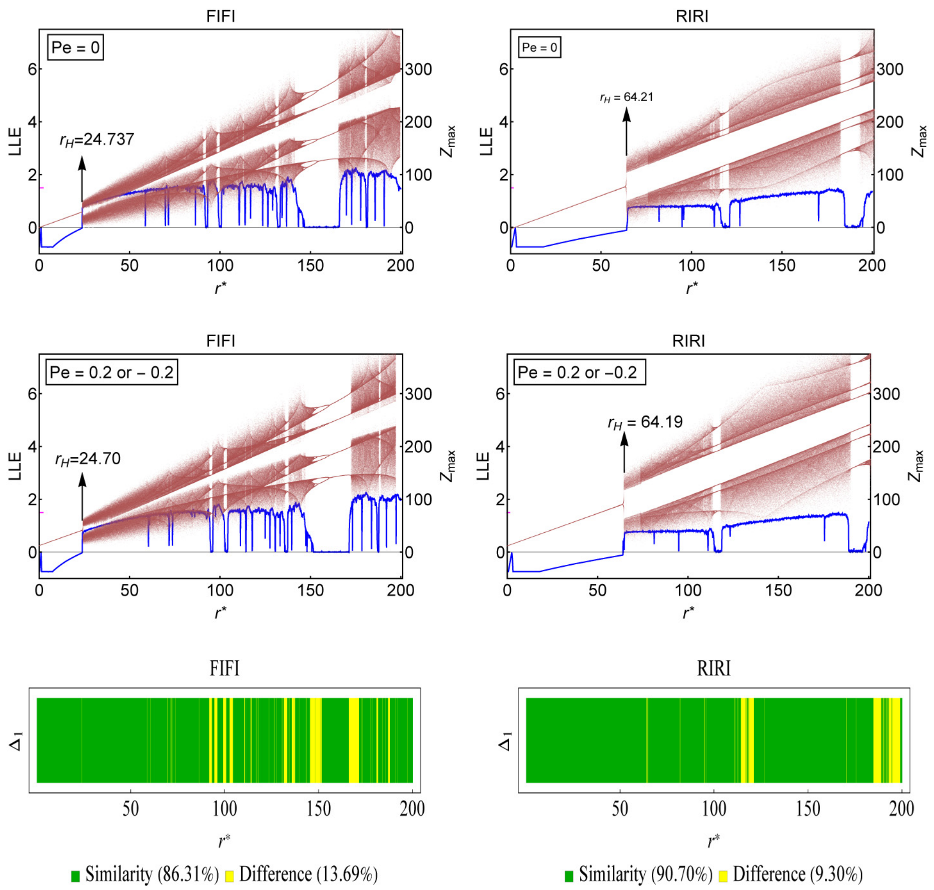

Fig. 4. Plot of the *LLE* and the bifurcation diagram versus r^* in the presence/absence of throughflow (both gravity-aligned and gravity-opposing cases) for symmetric boundaries with $Pr = 10$, $(X(0), Y(0), Z(0)) = (1, 1, 1)$ and $\Delta t = 0.0005$.

compared to FIFI and FIRI, and hence the similarity between the values of LLE is more. This is depicted by a 'similarity diagram' presented in Figs. 4 and 5 that uses the following definition. For two states i_1 and i_2,

$$\Delta_1 = \begin{cases} 0, & \text{if } sign(LLE, i_1) = sign(LLE, i_2) \\ 1, & \text{otherwise} \end{cases} \tag{44}$$

Now comparing the similarity and dissimilarity among the results of these boundaries shown in Fig. 6, as see that similarity is less between FIFI and RIRI boundaries compared to that between FIFI and FIRI. This is provided in the insets of Fig. 6 with the light yellow colour indicating the case of $\Delta_1 = 0$ and the dark green colour that of $\Delta_1 = 1$.

In order to find the influence of *Pe* on the periodic motion, we have considered the r^* interval of the largest periodic motion in Figs. 4 and 5, that concern symmetric and asymmetric boundaries respectively. Then a random value of r^* is picked from this interval and at this value of r^*, *Pe* is varied and the corresponding LLE is found using which Fig. 7 is plotted, where the difference state is defined as

$$\Delta_2 = \begin{cases} 0, & \text{if } LLE = 0 \\ 1, & \text{if } LLE > 0 \end{cases} \tag{45}$$

The light sky blue colour in Fig. 7 denotes $\Delta_2 = 0$ and the dark red corresponds to $\Delta_2 = 1$. When we vary *Pe* values in the considered range at this point of r^*, we observed that in the case of symmetric boundaries the system remains in the same periodic motion with the same periodicity (2 in the case of FIFI and 3 for RIRI), while in the case of asymmetric boundaries, only at certain values of *Pe* (*Pe* close to −0.2 and in the neighbourhood of 0) the system remains in periodic motion with periodicity 3.

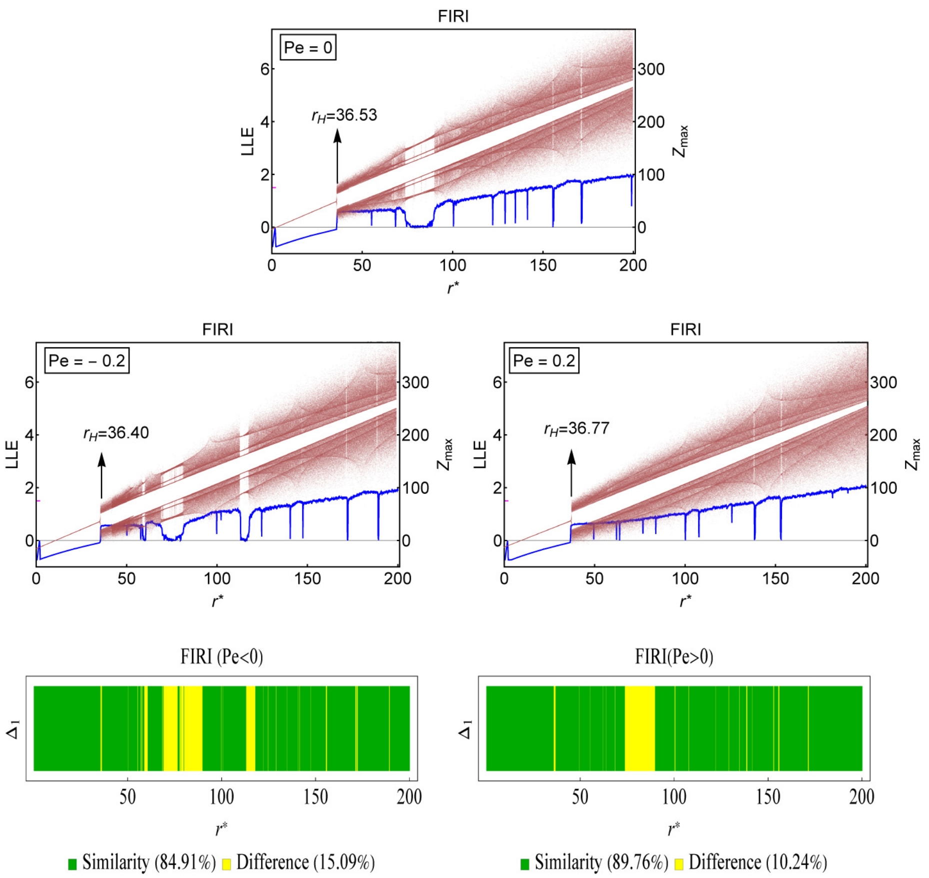

Fig. 5. Plots of *LLE* and the bifurcation diagram versus r^* in the presence/absence of throughflow (both gravity-aligned and gravity-opposing cases) for asymmetric boundaries, with $Pr = 10, (X(0), Y(0), Z(0)) = (1, 1, 1)$ and $\Delta t = 0.0005$.

Conclusion

The linear and weakly nonlinear stability analyses of axisymmetric convection in cylindrical enclosures is carried out. The aspect ratio in the range (0,7] is considered in the study. Using the Maclaurin series representation with a desired number of terms decided based on D Alembert's Root test, the axial eigenvalues are determined and its accuracy is considered acceptable by comparing the results in the limiting case of no throughflow of an earlier investigation, and an exact match is found. The influence of throughflow in gravity-aligned and gravity-opposing directions on linear and weakly nonlinear stability analyses of the considered problem has been reported. From this study we may drawn the following general conclusions:

(i) Irrespective of throughflow being gravity-aligned or gravity-opposing its impact on linear and weakly non-linear stability analyses remains the same for symmetric boundaries.
(ii) The influence of throughflow on onset depends on the nature of the boundaries.
(iii) In the case of symmetric boundaries, the influence of throughflow (irrespective of it is being gravity-aligned or gravity-opposing) is to stabilize the system.
(iv) In the case of asymmetric boundaries, the influence of gravity-aligned throughflow is to stabilize the system whereas gravity-opposing throughflow is destabilize the system.
(v) Influence of throughflow on r_H is exactly opposite to that of Ra_c.
(vi) In the case of symmetric boundaries, the influence of throughflow (irrespective of it is being gravity-aligned or gravity-opposing) is to pre-pone the appearance of chaos and post-pone the periodic motion.
(vii) In the case of asymmetric boundaries, the influence of gravity-aligned throughflow is to pre-pone the appearance of chaos and post-pone the periodic motion while the influence of gravity-opposing throughflow is to post-pone the appearance of chaos and suppress the periodic motion.

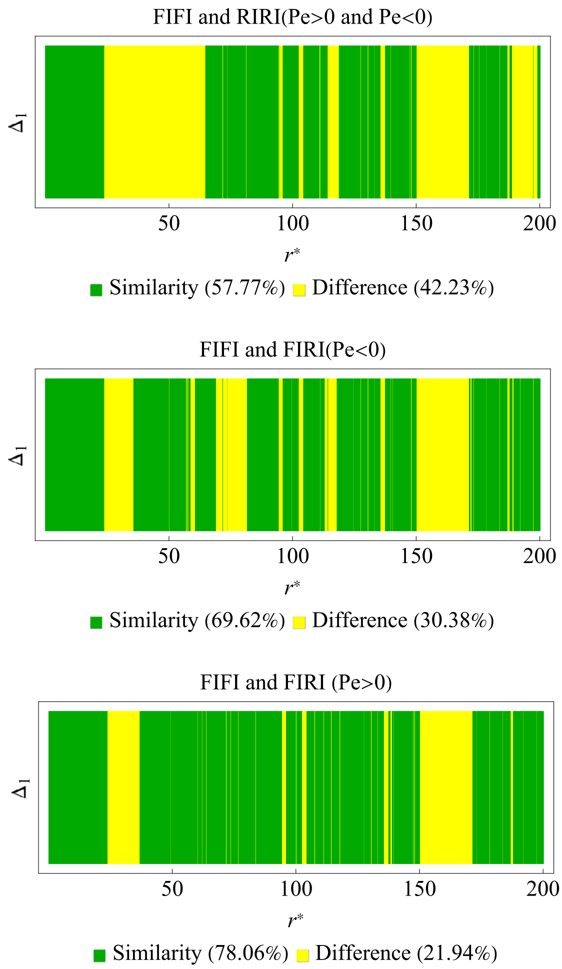

Fig. 6. The difference plots between the boundaries in the presence of throughflow.

CRediT authorship contribution statement

P.G. Siddheshwar: Conceptualization, Methodology, Visualization, Investigation, Supervision, Validation, Review & editing. **Kanchana C.:** Software, Data curation, Visualization, Writing – original draft. **L.M. Pérez:** Software, Data curation, Visualization, Writing – original draft. **D. Laroze:** Visualization, Investigation, Supervision, Validation, Review & editing.

Declaration of competing interest

The authors declare that they have no known competing financial interests or personal relationships that could have appeared to influence the work reported in this paper.

Data availability

No data was used for the research described in the article.

Acknowledgements

This work is dedicated to one of the authors (PGS) as a celebration of his 65th birthday. KC is grateful to the Universidad de Tarapacá, Chile, for supporting her research work. LMP acknowledges financial support from ANID through Convocatoria Nacional Subvención a Instalación en la Academia Convocatoria Año 2021, Grant SA77210040.

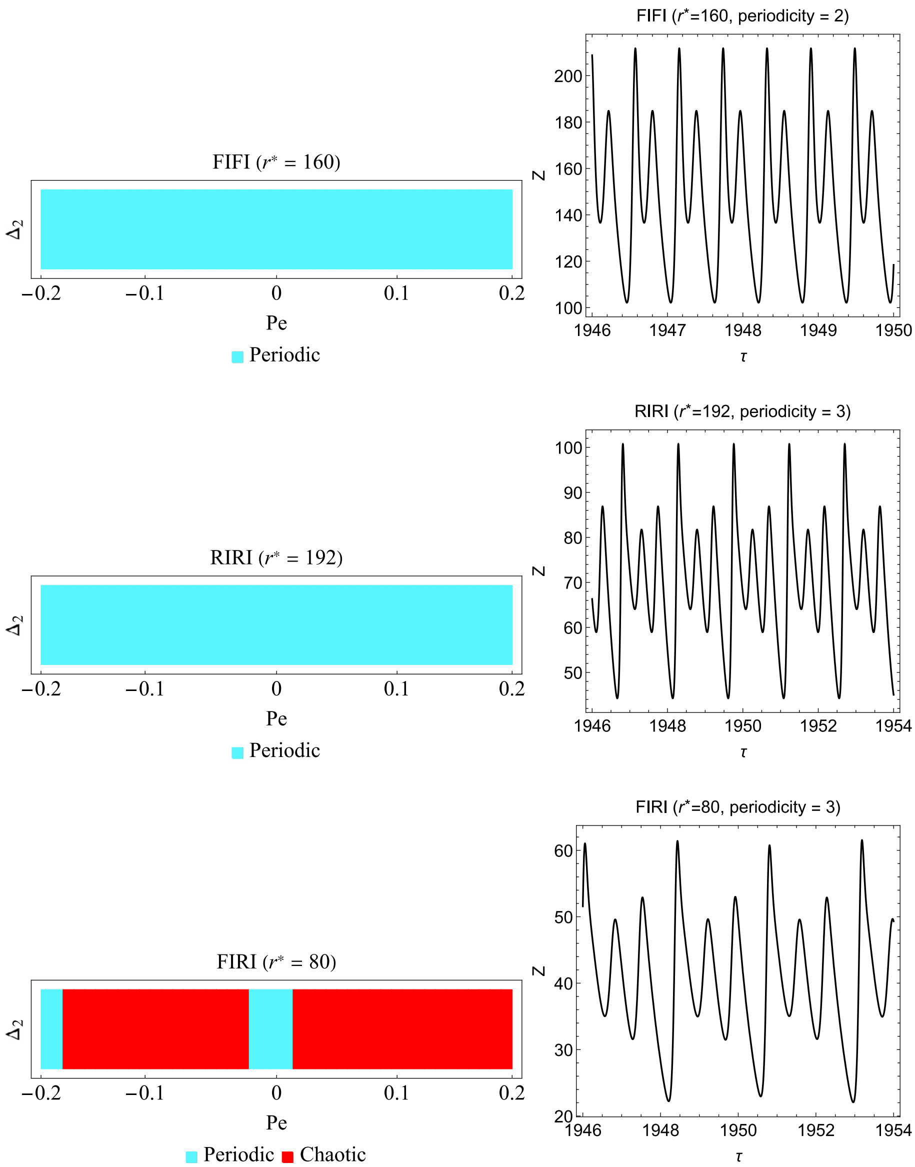

Fig. 7. LLE values for different values of *Pe* at a particular value of r^* (chosen in the first largest periodic interval of LLE plots) for different boundaries.

References

[1] Rayleigh L. On convection currents in a horizontal layer of fluid when the higher temperature is on the under side. Lond Edinb Dublin Philos Mag J Sci 1916;32:529–46.
[2] Pellew A, Southwell RV. On maintained convective motion in a fluid heated from below. Proc R Soc A 1940;176:312–43.
[3] Soberman RK. Effects of lateral boundaries on natural convection. J Appl Phys 1958;29:872–3.
[4] Yih C. Thermal instability of viscous fluids. Quart Appl Math 1959;17:25–42.
[5] Ostrach S, Pnueli D. The thermal instability of completely confined fluids inside some particular configurations. ASME J Heat Transfer 1963;85:346–54.
[6] Catton I, Edwards DK. Initiation of thermal convection in finite right circular cylinders. AIChE J 1970;16:594–601.
[7] Liang SF, Vidal A, Acrivos A. Buoyancy-driven convection in cylindrical geometries. J Fluid Mech 1969;36:239–58.
[8] Charlson GS, Sani RL. Thermoconvective instability in a bounded cylindrical fluid layer. Int J Heat Mass Transfer 1970;13:1479–96.
[9] Stork K, Müller U. Convection in boxes: an experimental investigation in vertical cylinders and annuli. J Fluid Mech 1975;71:231–40.
[10] Brown SN, Stewartson K. On finite amplitude benard convection in a cylindrical container. Proc R Soc A 1978;360:455–69.
[11] Wang BF, Ma DJ, Chen C, Sun DJ. Linear stability analysis of cylindrical Rayleigh–Bénard convection. J Fluid Mech 2012;711:27–39.
[12] Yu J, Goldfaden A, Flagstad M, Scheel JD. Onset of Rayleigh-Bénard convection for intermediate aspect ratio cylindrical containers. Phys Fluids 2017;29:024107.
[13] Li PX, Li BW, Chen L, Leng XY, Luo XH, Yu Y, et al. 3D DNS of laminar Rayleigh-Bénard convection in a cylinder for incompressible fluid flow. Chinese J Phys 2022;79:374–94.

[14] Riehl H. Tropical meteorology. New York: McGraw-Hill; 1954 [Chapter 1-2].
[15] Augstein E, Schmidt H, Ostapoff F. The vertical structure of the atmosphere planetary boundary layer in undisturbed trade winds over the Atlantic ocean. Bound Layer Meteors 1974;6:129–50.
[16] Krishnamurti R. On cellular cloud patterns. Part 1: Mathematical model. J Atmos Sci 1975;32:1353–63.
[17] Gershuni GZ, Zhukhovitskii EM, Shvartsblat DL. On the stability of transverse flow of fluid between permeable boundaries. J Appl Math Mech 1968;32:266–71.
[18] Shvartsblat DL. The spectrum of perturbations and convective instability of a plane, horizontal fluid layer with permeable boundaries. J Appl Math Mech 1968;32:276–81.
[19] Nield DA. Throughflow effects in the Rayleigh-Bénard convective instability problem. J Fluid Mech 1987;185:353–60.
[20] Capone F, Gianfrani JA, Massa G, Rees DAS. A weakly nonlinear stability analysis of the effect of vertical throughflow on Darcy-Bénard convection. Phys Fluids 2023;35:014107.
[21] Barletta A, Storesletten L. Onset of convection in a vertical porous cylinder with a permeable and conducting side boundary. Int J Therm Sci 2015;97:9–16.
[22] Brandão PV, Celli M, Barletta A, Storesletten L. Thermally unstable throughflow of a power-law fluid in a vertical porous cylinder with arbitrary cross-section. Int J Therm Sci 2021;159:106616.
[23] Lorenz EN. Deterministic nonperiodic flow. J Atmos Sci 1963;20:134–41.
[24] Sparrow C. The Lorenz equations: Bifurcations, chaos, and strange attractors. New York: Springer Verlag; 1982.
[25] Kanchana C, Su Y, Zhao Y. Regular and chaotic Rayleigh-Bénard convective motions in methonol and water. Commun Nonlinear Sci Numer Simul 2020;83:105129.